

**Vibrational Structure in Magnetic Circular Dichroism Spectra of Polycyclic Aromatic Hydrocarbons**

**Jakub Kaminský,<sup>#</sup> Jakub Chalupský,<sup>#</sup> Petr Štěpánek,<sup>§</sup> Jan Kříž<sup>#</sup> and Petr Bour<sup>##\*</sup>**

*<sup>#</sup>Institute of Organic Chemistry and Biochemistry, Academy of Sciences, Flemingovo náměstí 2,  
16610 Prague, Czech Republic.*

*<sup>§</sup>NMR Research Unit, Faculty of Science, University of Oulu, PO Box 3000, 90014 Oulu, Finland*

\* bour@uochb.cas.cz

## **Abstract**

Absorption (ABS) and magnetic circular dichroism (MCD) spectroscopies are powerful and simple methods to discriminate among various compounds. Polycyclic aromatic hydrocarbons (PAHs) provide particularly strong signal, which, for example, facilitates their detection in the environment. However, interpretation of the spectra is often based on quantum-chemical simulations, providing a limited precision only. In the present work, we use time-dependent density functional theory (TDDFT) and complete active space second-order perturbation theories (CASPT2) to understand spectral features observed in a series of naphthalene, anthracene, phenanthrene, and three larger compounds. The electronic computations provided reasonable agreement with the experiment for the smaller molecules, while a large error persisted for the bigger ones. However, many discrepancies could be explained by vibrational splitting of the electronic transitions across the entire spectral range. Compared to plain absorption, MCD spectral bands and their vibrational splitting were more specific for each aromatic molecule. The computational tools allowing simulations of detailed vibrational features in the electronic spectra thus promise to open a qualitatively new chapter in the spectroscopy of aromatic compounds.

## Introduction

Polycyclic aromatic hydrocarbons (PAHs) are omnipresent in chemistry and industry. As such, they are also principal environmental pollutants and serious concerns have been expressed regarding their effect on human health. This brings the need to detect and identify them quickly and efficiently. A wide range of methods is traditionally used for this purpose including nuclear magnetic resonance, mass spectroscopy and high-performance liquid and gas chromatography. Because some of these methods are destructive, presume extraction using toxic organic solvents or require long operating times, faster and more environment-friendly optical spectroscopic techniques are explored. For example, fluorescence and multiphoton microscopy have been proposed to determine PAH content in plants. Absorption and fluorescence spectroscopies also established as simpler methods for PAHs' characterization as these molecules exhibit rich spectral features with the wavelength range accessible to the spectrometers.<sup>7</sup>

By definition, the amount of structural information obtained from the low-resolution spectral techniques is limited. However, it can be increased if complemented by the magnetic circular dichroism (MCD) spectroscopy. MCD measures difference in absorption of left- and right-circularly polarized light in a static magnetic field. The differential spectra are in principle more variable and more sensitive to the chemical structure than total absorption. PAHs are ideal systems to be studied by this technique as they provide strong and variable MCD signal, depending on molecular structure including chemical substitution or replacement of an aromatic carbon by heteroatom. This is also the case for other frequent carbon "nanomaterials", fullerenes, where we and others applied this technique to discriminate otherwise chemically very similar species.

Modern molecular applications of MCD started in 1960s when appropriate instrumentation was broadly available.<sup>9</sup> At about the same time, Stephens' quantum-mechanical MCD theory provided expressions readily usable in spectral simulations, which in turn could be used as a solid basis for interpretation of the spectra. Yet many problems needed to be overcome, such as the need to work with imaginary wavefunction and the dependence of calculated MCD intensities on coordinate origin. Suitable computer programs available to a broader public appeared thus only in the last decade. Typically, they are based on the response theory; other implementations include the complex polarization propagator<sup>23</sup> and real-time propagation of the wave function.<sup>24</sup>

At the present study we use the sum over state (SOS) method and time-dependent density functional theory (TDDFT) wavefunctions for generation of MCD intensities. This approach makes it possible to include a big number of excited electronic states and calculate large molecules in a reasonable time. Alternatively, computationally more costly but parameter-free complete active space second-order perturbation theory (CASPT2)<sup>27</sup> and explicit inclusion of the magnetic operator

to the Hamiltonian<sup>28</sup> are used to generate excited electronic states and absorption and MCD intensities. These methods are recently capable to provide theoretical predictions even for larger PAHs studied herein due to the dramatic efficiency improvements achieved by the density matrix renormalization group (DMRG)<sup>29</sup> theory. In our case, they also provide a precious feedback both on the accuracy of TDDFT and reliability of MCD simulations, at least for the  $\pi$ -transitions that could be fully included in the CASPT2 Hamiltonian.

In spite of the advances of computational chemistry, a band-to-band comparison of calculated and experimental spectra is still problematic, especially for larger PAHs. As shown below, however, many discrepancies can be explained by electronic-vibrational interactions. In fact, vibrational splitting of the electronic bands is a typical feature encountered in spectra of PAHs and aromatic molecules in general. This phenomenon was relatively difficult to interpret in the past.<sup>32</sup> Fortunately, modern computational tools including efficient algorithms for computation of the Franck-Condon factors allow to simulate vibrational features at the same level as the electronic ones.

Owing to these theoretical advances, the vibrational “distortion” of the spectra becomes a welcome spectroscopic mark often allowing better distinguishing of various molecular species. The vibrational patterns can also be used to confirm assignment of experimental and calculated transitions, which can be particularly difficult for larger molecules. For example, a systematic TDDFT error dependent on polarization of the transitions was observed for long polycenes.<sup>40</sup> In the present study, a series of six compounds of variable size is included that allows for a detailed computational analysis and assess the advantages but also the limits of the spectroscopic and computational approaches.

## Methods

The samples were obtained from the Institute of Chemical Process Fundamentals (Prague). Experimental MCD and absorption spectra of the compounds (**Figure 1**) were measured in *n*-hexane solutions on a JASCO J-815 (Japan) spectrometer equipped with permanent magnet (1.5 tesla). Five PAHs were available as a racemic mixture, only PAH 6 ([6]helicene) was on a pure P-enantiomeric form. The nonpolar solvent was chosen to minimize the effect of environment on the spectra. Used pathlengths and concentrations are summarized in **Table S1** in the Supporting Information. Scanning speed was set to 20 nm/min, temperature 20°C, accumulation time 8 seconds per point; averages of three scans are plotted.

Geometries of all compounds were optimized by energy minimization at the B3LYP/6311++G\*\* approximation level, using the Gaussian program.<sup>41</sup> For some simulations the polarizable

continuum model (PCM)<sup>42</sup> with *n*-hexane parameters was used to account for the environment. Note nevertheless that solvent effects in PAHs' electronic spectra are rather minor;<sup>43</sup> our vacuum and PCM results were also quite similar. The TDDFT computations of electronic transition energies and intensities were performed in Gaussian using three DFT functionals (B3LYP,  $\omega$ B97XD and LC-BLYP) and the 6-311++G\*\* basis set. With other functionals (CAM-B3LYP and  $\omega$ B97X) standard and simplified Tamm-Dancoff approximations<sup>44</sup> were also tested, using the sTD program (<https://www.chemie.uni-bonn.de/pctc/mulliken-center/software/stda/stda>). B3LYP and other hybrid functionals were applied because of their previous good performance for similar problems, on LC-BLYP we wanted document the effect of the GGA approximation,<sup>46</sup> and the sTD approach was explored as a way allowing to treat larger molecules.<sup>44</sup>

MCD spectra were generated from TDDFT excited states (not only the orbitals). Faraday *B*-term for each  $n \rightarrow j$  electronic transition was calculated as<sup>26</sup>

$$B = \text{Im} \mu_{nj,\alpha} \varepsilon_{\alpha\beta\gamma} T_{nj,\beta\gamma} \quad (1)$$

where

$$\begin{aligned} T_{nj,\beta\gamma} = & \sum_{k \neq n} \frac{\mu_{jk,\beta} m_{kn,\gamma}}{E_{kn}} + \sum_{k \neq j} \frac{\mu_{kn,\beta} m_{jk,\gamma}}{E_{kj}} \\ & - \frac{i \varepsilon_{\gamma\delta\varepsilon}}{4N_e} \left[ \sum_{k \neq n} \mu_{jk,\beta} \left( \sum_{l \neq n} \frac{\mu_{kl,\delta} \nabla_{ln,\varepsilon}}{E_{ln}} + \sum_{l \neq k} \frac{\mu_{ln,\delta} \nabla_{kl,\varepsilon}}{E_{kl}} \right) \right. \\ & \left. + \mu_{kn,\beta} \sum_{k \neq j} \left( \sum_{l \neq k} \frac{\mu_{jl,\delta} \nabla_{lk,\varepsilon}}{E_{kl}} + \sum_{l \neq j} \frac{\mu_{lk,\delta} \nabla_{jl,\varepsilon}}{E_{lj}} \right) \right] \end{aligned} \quad (2)$$

$\mu_{nj,\alpha} = \langle n | \mu_\alpha | j \rangle$  is  $\alpha$ -coordinate of the transition dipole moment element, similarly for the magnetic dipole moment  $\mathbf{m}$  and the gradient  $\nabla$ ,  $\varepsilon_{\alpha\beta\gamma}$  is the anti-symmetric tensor,  $E_{kn} = E_k - E_n$  is difference of electronic energies and  $N_e$  is the number of electrons. Einstein summation convention is followed, i.e. Cartesian coordinate index occurring twice in a product is summed over all possible values, and atomic units are used. In (2) we used the origin-independent ‘‘LORG’’ (localized orbital/local origin)<sup>26</sup> expression of the ‘‘MCD tensor’’<sup>35</sup>  $\mathbf{T}_{nj}$ . Note that enantiomers provide the same MCD: the coordinate inversion changes only signs of the electric dipole moments or gradients, which always multiply to unity in the expression for *B*. Degenerate electronic levels, conventionally giving rise to

Faraday *A*-terms, were included as a limit of close-lying states,<sup>47</sup> i.e., by replacing expressions  $\frac{1}{E_{ab}}$

by  $\frac{E_{ab}}{E_{ab}^2 + \Gamma^2}$ , where  $\Gamma = 0.01$  a.u. The GUVUDE program interfaced to Gaussian and sTD was

used for the MCD simulations.

Alternatively to TDDFT, single- and multi-state complete active space second-order perturbation theories (SS-CASPT2<sup>27</sup> and MS-CASPT2,<sup>48</sup> respectively) were used to obtain the ground and excited electronic states. MCD intensities were calculated using the method of Ganyushin and Neese.<sup>28</sup> The ANO-L-VTZP basis set was employed,<sup>49</sup> complete active space self-consistent field (CASSCF)<sup>50</sup> reference wavefunctions were calculated in localized ground-state CASSCF orbitals. Active spaces (CAS)/number of electronic states included were (10,10)/15 (naphthalene), (14,14)/17 (anthracene), (14,14)22 (phenanthrene), (18,18)/25 (PAH4), (22,22)/24 (PAH5) and CAS(26,26)/25 (PAH6). CASs comprised all  $\pi$  electrons and orbitals. The density matrix renormalization group (DMRG) algorithm was used as a solver for the configuration interaction (CI) part of CASSCF, and cumulant approximation to the four-electron reduced density matrices was used.<sup>52</sup> Number of DMRG renormalized basis functions was set to 512 in all cases. Ionization potential and electron affinity<sup>53</sup> and imaginary<sup>54</sup> level shifts of 0.25 and i0.2, respectively, were applied to avoid the intruder-state problem in CASPT2. These calculations were performed using program ORZ and Block DMRG routines (<https://github.com/sanshar/Block>). The MS-CASPT2 method was used for the three smaller molecules (naphthalene-phenanthrene), while only the computationally cheaper SS-CASPT2 procedure could be used for the larger PAHs.

Vibrational substructure of selected electronic transitions was calculated within TDDFT and harmonic approximation. The transition electric dipole moment<sup>38</sup> and MCD tensor<sup>35</sup> were expanded to the first order with respect to nuclear coordinates

$$X(R) = X(0) + \sum_{\lambda,\alpha} \frac{\partial X}{\partial R_{\alpha}^{\lambda}} \Delta R_{\alpha}^{\lambda} \quad (3)$$

where  $\Delta R_{\alpha}^{\lambda}$  is deviation of  $\alpha$ -coordinate of atom  $\lambda$  from its equilibrium position. The Cartesian tensor derivatives  $\frac{\partial X}{\partial R_{\alpha}^{\lambda}}$  were obtained numerically by a two-step differentiation (0.01 Å in each

direction) and transformed to vibrational normal mode coordinates  $Q_J$ , as  $\frac{\partial X}{\partial Q_J} = \sum_{\alpha=1}^3 \sum_{\lambda=1}^{N_{at}} \frac{\partial X}{\partial R_{\lambda\alpha}} S_{\lambda\alpha}^J$ ,

where  $S$  is the Cartesian-normal mode transformation matrix. The default Gaussian differentiation step (0.001 Å) produced nearly the same results. B-terms corresponding to transitions among vibrational levels of the electronic ground and excited states were calculated as

$$B(\mathbf{v}_n \rightarrow \mathbf{v}_j) = \text{Im} \langle \mathbf{v}_n | \boldsymbol{\mu}_{n_j,\alpha} | \mathbf{v}_j \rangle \boldsymbol{\epsilon}_{\alpha\beta\gamma} \langle \mathbf{v}_n | T_{n_j,\beta\gamma} | \mathbf{v}_j \rangle \quad (4)$$

Only transitions from the vibrational ground state ( $\mathbf{v}_n = 0$ ) were considered. As pointed out earlier,<sup>57</sup> this approach provides a reasonable basis for reproducing the MCD vibrational structure including both the Franck-Condon and Herzberg-Teller contributions.<sup>35</sup>

## Results and Discussion

**TDDFT and CASPT2 Performance.** Transition energies and oscillator strengths calculated by the B3LYP (vacuum), B3LYP/CPCM,  $\omega$ B97XD/CPCM, LC-BLYP/CPCM and CASPT2 (vacuum) methods are compared to experimental data in **Tables 1** and **2**. For naphthalene (**Table 1**) all 20 lowest-energy transitions are included. For the larger systems (**Table 2**) experimentally-assignable or lowest-energy ones are listed only; other TDDFT transitions are listed in **Table S2** in Supporting Information. In general, the accuracy of TDDFT and CASPT2 energies is similar as in the previous studies. For naphthalene, the CASPT2 gives a small average absolute deviation of energies ( $\Delta = 0.44$  eV), and the B3LYP functional provides very close results ( $\Delta = 0.37$  eV). As expected, the solvent represented by PCM brings about only very minor changes of the vacuum results. The more modern  $\omega$ B97XD functional<sup>62</sup> with  $\Delta = 0.75$  eV gives spectral parameters rather inferior to those obtained by the older B3LYP. The simpler GGA LC-BLYP method gives the largest error of 1.02 eV.

For the larger molecules (**Table 2**) statistical performances of B3LYP and CASPT2 are comparable ( $\Delta$  of 0.21 versus 0.23 eV). The smaller values of the errors may be caused by a smaller number of experimental states available for comparison. The relative improvement of the B3LYP results may be partially caused by the fact that only  $\pi$ - $\pi^*$  transitions could be included within CASPT2, which is not sufficient for higher-energy transitions. On the other hand, this CASPT2 limitation does not seem to be critical within the spectral interval of interest ( $\sim 200$ -400 nm), where it provides a reasonable overall agreement with the best TDDFT computations. One should also be aware that experimental results may vary across different studies; for example seven (!) different energy values for the first naphthalene transition were compiled in reference <sup>63</sup>. This is caused by different measurement conditions (vacuum versus solvent, etc.), varying experimental accuracy and some assignment uncertainties are related to the vibrational substructure of the bands discussed below.

**MCD and Absorption Spectral Intensities.** The experimental and calculated spectra are plotted in **Figures 2** (naphthalene, five computational levels) and **3** (other molecules, sTD, B3LYP and CASPT2). The experiment is consistent with previous works, such as MCD studies on naphthalene,<sup>64</sup> anthracene,<sup>11</sup> phenanthrene,<sup>11</sup> and absorption spectra of PAHs 4-6.<sup>59</sup> For PAH6, where a pure enantiomer was available, electronic (natural) circular dichroism spectrum was measured and is plotted in **Figure S1**. It is not analyzed further as this can be found in Ref. <sup>59</sup>.

The experimental naphthalene absorption spectrum in the region accessible to the spectrometer is relatively simple, with a strong band at 220 nm and a weaker signal within 250-300

nm (**Figure 2**). This is more or less reproduced by all the computational methods. The MCD spectrum is dominated by a +/- (if seen from left to right) couplet around 200 nm, reproduced by all methods except sTD, although the theoretical intensities vary significantly. Within 250 - 300 nm the MCD signal is very structured and mostly negative. CASPT2 thus provides perhaps the best agreement, including a weak positive signal above 300 nm.

Computed absorption spectra of other molecules reproduce the principal experimental features, too, although resemblance to the experiment deteriorates with molecular size (**Figure 3a**). For example, the most intense band, experimentally at  $\sim 250$  nm for anthracene and phenanthrene, shifts right to longer wavelength and its intensity significantly diminishes for PAH5-6. This is reproduced by the theory, although the B3LYP method overestimates the shift, predicting transition number 3 at 350 nm for PAH6, while the experimental maximum occurs at  $\sim 320$  nm. Also, as pointed out previously, TDDFT provides rather uneven precision in energies for various types of transitions, such as those polarized along the shorter and longer molecular axis (referred to as " $L_a$ " and " $L_b$ ", respectively).<sup>65</sup> This complicates the assignment particularly in the short-wavelength region where the density of the states is large. The CASPT2 method gives a smaller shift of the main band, closer to experiment, but underestimates its wavelength. It also predicts rather unrealistic PAH4-6 spectral shapes below 250 nm.

Similarly as for the absorption, the simulations reasonably well reproduce experimental MCD spectra (**Figure 3b**) of anthracene and phenanthrene, while for PAH4-6 a band-to-band assignment of calculated and measured curves is impossible. PAH4 and 5 are perhaps the worst examples, whereas at least some correspondence between theory and experiment (e.g., for bands 3 and 12) exists for PAH6. We explain the modest agreement by a higher sensitivity of MCD to computational error; for example close-lying bands of opposite MCD signs dramatically change the resultant spectrum even for a small change in their position. Another source of the discrepancies may be the vibrational splitting discussed below.

**Vibrational Structure of Lowest-Energy Electronic Transitions.** The vibrational splitting of electronic bands is documented on naphthalene, anthracene and phenanthrene, where the lowest-energy transitions are not overlapped and can be calculated with affordable computational cost. Note that computation of vibrationally-resolved MCD intensities requires computationally demanding numerical differentiation of the transition (MCD) tensor.<sup>35</sup> Vibrationally-resolved absorption alone can be calculated much faster owing to the analytical implementation<sup>66</sup> available in Gaussian lately.<sup>67</sup>

The simulation methodology for the vibrational structure is feasible for cases when the geometries of the electronic ground and excited states are similar.<sup>38</sup> This is true for the  $\pi$ - $\pi^*$  excitations in PAHs; the extent of the geometric changes is documented for the  $S_1$  and  $S_2$  states of

naphthalene in **Table 3**. Indeed, the C-H bond lengths remain virtually the same. The C-C bond lengths become both shorter and longer, but the relative changes do not exceed 4 %. Behavior of the other molecules is similar (**Table S3**) and corresponds to changes previously seen in excited states of benzene<sup>45</sup> or PAH6 ([6] helicene).<sup>39</sup>

In naphthalene, for example, we can identify vibrational structure of the first and second lowest-energy electronic bands (**Figure 4**). Although the energy ordering of these two transitions ( $B_{3u}$  and  $B_{2u}$ , **Table 2**) is predicted by different methods differently, it can be well-established on the basis of characteristic vibrational patterns. The  $B_{3u}$  band is covering a wide range of about 240-290 nm. Vibrational sub-bands of the weaker  $B_{2u}$  transition are observed on its shoulder, within a narrower interval of  $\sim$  290-310 nm. The vibrational absorption structure is reasonably well predicted by the simulation allowing to assign the strongest vibrational bands (**Figure 4**, right). Not surprisingly, they comprise ring vibrations (e.g. modes 10 and 9' involving bond length changes), both symmetric ( $A_g$ ) and asymmetric (e.g.,  $B_{1g}$ ), relevant to the geometry variations (**Table 3**, selected vibrational transitions are also listed in **Table S4**). Correspondence of the simulated MCD patterns to the experiment is less obvious, and the positive signal of the 0-0' transition (number 1 in the figure) is not predicted at all. Other signs and overall patterns do agree and most of the MCD bands can also be related to the absorption ones.

Similarly spectacular is the vibrational pattern of the  $S_0 \rightarrow S_1$  ( $B_{1u}$ ) transition in anthracene plotted in **Figure 5**. The electronic transition occurs for higher wavelength and the visible vibrational splitting is wider than for naphthalene, approximately within 300-380 nm. The calculation fairly well reproduces the absorption, allowing assigning all the eight most-intense vibrational sub-bands. Also the negative character of the MCD signal is well-reproduced. However, as pointed out in Ref. [11](#), around 350 nm another transition ( $S_0 \rightarrow S_2$ ,  $B_{2u}$ ) interferes in MCD. Its bi-signed MCD signal is even more intense than for  $S_0 \rightarrow S_1$ , although it is not visible in the absorption. The simulation predicts this only qualitatively: while the calculated dissymmetry factor (ratio of MCD to absorption) is rather low for  $S_0 \rightarrow S_1$ ,  $\sim 1.4 \times 10^{-3}$ , it is much larger for  $S_0 \rightarrow S_2$ ,  $\sim 1.5 \times 10^{-2}$ . Therefore, MCD of the second transition is much more pronounced than the absorption. Vibrational resonance between the two electronic states may further boost the MCD signal,<sup>57</sup> but this is currently not implemented in the simulations.

For the  $S_0 \rightarrow S_1$  transition of phenanthrene (**Figure 6a**) we see again a reasonable agreement between the simulation and theory. Minor signals predicted between bands 1 and 2, and 3 and 4 are not resolved experimentally. A positive MCD experimental signal between bands labeled as 3 and 4 is not reproduced, otherwise the simulation well captures the overall negative character of the observed spectrum.

Vibrational structure of the second  $S_0 \rightarrow S_2$  absorption and MCD phenanthrene band is analyzed in **Figure 6b**. This band strongly overlaps with the  $S_0 \rightarrow S_1$  signal; nevertheless about four vibrational sub-bands can be recognized. They are more resolved in the experimental absorption spectrum, whereas the experimental MCD is quite noisy.

**Vibrational Structure in Larger PAHs.** Similar analysis of vibrational features in MCD spectra of the largest PAHs was prevented by a high density of mutually overlapping electronic states. Theoretical simulations were somewhat hampered by extensive computational time and numerical instabilities. Nevertheless, the computations indicate the importance of the vibrational splitting for reproduction of the experimental patterns. For PAH4 and naphthalene we computed the vibrational-electronic absorption spectra across a wider range of wavelength as shown in **Figure 7**. Ten and fifteen electronic excited states were included for naphthalene and PAH4, respectively, and their contributions are plotted individually. Although some states may be missing due to the lack of convergence the spectra involving vibrational splitting do reproduce the experiment much better than the electronic ones alone (cf. **Figure 2** and **3a**). For higher-excited electronic states (e.g., number 9 in naphthalene, see **Figure S2** for its MCD, and 4 in PAH4) we can also observe a more “classical” absorption profiles than for the lower-energy ones. That means that the “0-0” transition between vibrational ground states is the most intense one, and intensity of the others monotonically decreases with higher energy (shorter wavelength).

## Conclusions

We have explored several theoretical approaches to simulate absorption and MCD spectra of model polycyclic aromatic hydrocarbons, with a long term objective to make spectroscopic detection of these compounds more reliable. Hybrid density functionals were in general found capable to reproduce the main spectral features, but the accuracy varied, in particular for absorption and MCD intensities. The CASPT2 results were consistent with those obtained with the hybrid functional. Thus although the wavefunction method is technically more advanced, it did not bring a qualitatively better agreement with experiment for the studied system. However, a large part of the discrepancies between the experiment and theory could be explained by vibrational splitting of the electronic bands. This was rather ignored in previous studies, sometimes even leading to erroneous assignment of electronic bands. The present study shows that the vibrational structure can be to a large extent rationalized by the simulations, and that it is necessary to involve understanding PAHs’ spectroscopic responses. Then individual compounds give quite specific vibrational MCD and absorption features that can be used for their identification. Yet the computational tools need to be improved in the future to be able to tackle large molecules more reliably.

## Acknowledgement

The work was supported by the Grant Agency of the Czech Republic (Grant No. 15-19143S, 16-05935S to PB, and 16-00270S to JK). Computational resources were provided by the CESNET LM2015042 and the CERIT Scientific Cloud LM2015085. We thank Dr. Jan Sýkora (Inst. Chemical Process Fundamentals) for providing us with the compounds.

## Supporting Information

Further computational tests, details about electronic transitions, such as ECD spectrum of PAH6 and MCD spectrum of 9<sup>th</sup> naphthalene band. This information is available free of charge via the Internet at <http://pubs.acs.org>.

## References

1. Abdel-Shafy, H. I.; Mansour, M. S. M. A Review on Polycyclic Aromatic Hydrocarbons: Source, Environmental Impact, Effect on Human Health and Remediation. *Egypt. J. Petroleum* **2016**, *25*, 107-123.
2. Kim, K. H.; Jahan, S. A.; Kabir, E.; Brown, R. J. C. A Review of Airborne Polycyclic Aromatic Hydrocarbons (PAHS) and Their Human Health Effects. *Environ. Int.* **2013**, *60*, 71-80.
3. Alves, W. S.; Manoel, E. A.; Santos, N. S.; Nunes, R. O.; Domiciano, G. C.; Soares, M. R. Detection of Polycyclic Aromatic Hydrocarbons (PAHS) in Medicago Sativa L. By Fluorescence Microscopy. *Micron* **2017**, *95*, 23-30.
4. Banjoo, D. R.; Nelson, P. K. Improved Ultrasonic Extraction Procedure for the Determination of Polycyclic Aromatic Hydrocarbons in Sediments. *J. Chromatogr. A* **2005**, *1066*, 9-18.
5. Lau, E. V.; Gan, S.; Ng, H. K. Extraction Techniques for Polycyclic Aromatic Hydrocarbons in Soils. *Int. J. Anal. Chem.* **2010**, 1-9.
6. Wild, E.; Dent, J.; Thomas, G. O.; Jones, K. C. Visualizing the Air-to-Leaf Transfer and within-Leaf Movement and Distribution of Phenanthrene: Further Studies Utilizing Two-Photon Excitation Microscopy. *Environ. Sci. Technol.* **2006**, *40*, 907-916.
7. Hendecourt, L.; Ehrenfreund, P. Spectroscopic Properties of Polycyclic Aromatic Hydrocarbons (PAHS) and Astrophysical Implications. *Adv Space Res.* **1997**, *19*, 1023-1032.
8. Michl, J. Magnetic Circular Dichroism of Aromatic Molecules. *Tetrahedron* **1984**, *40*, 3845-3934.

9. Mason, W. R. *A Practical Guide to Magnetic Circular Dichroism Spectroscopy*. Wiley-Interscience: Portland, 2007.
10. Stephens, P. J. Theory of Magnetic Circular Dichroism. *J. Chem. Phys.* **1970**, *52*, 3489-3516.
11. Steiner, R. P.; Michl, J. Magnetic Circular Dichroism of Cyclic  $\Pi$ -Electron Systems. 11. 1 Derivatives and Aza Analogues of Anthracene. *J. Am. Chem. Soc.* **1978**, *100*, 6861-6867.
12. Whipple, M. R.; Vařák, M.; Michl, J. Magnetic Circular Dichroism of Cyclic  $\pi$ -Electron Systems. 8. <sup>1,2</sup> Derivatives of Naphtalen. *J. Am. Chem. Soc.* **1978**, *100*, 6844-6852.
13. Weeks, G. H.; Adcock, W.; Kllngensmith, K. A.; Waluk, J. W.; West, R.; Vaak, M.; Downing, J.; Michl, J. A Probe for Substituent Hyperconjugative Power: MCD (Magnetic Circular Dichroism) of the Benzene L<sub>b</sub> Band. *Pure Appl. Chem.* **1986**, *58*, 39-53.
14. Štěpánek, P.; Straka, M.; Šebestík, J.; Bouř, P. Magnetic Circular Dichroism of Chlorofullerenes: Experimental Andcomputational Study. *Chem. Phys. Lett.* **2016**, *647*, 117-121.
15. Gasyna, Z.; Schatz, P. N.; Hare, J. P.; Dennis, T. J.; Kroto, H. W.; Taylor, R.; Walton, D. R. M. The Magnetic Circular Dichroism and Absorption Spectra of C<sub>60</sub> Isolated in Ar Matrices. *Chem. Phys. Lett.* **1991**, *183*, 283-291.
16. Pilch, M.; Pawlikowski, M.; Mortensen, O. S. Magnetic Circular Dichroism (MCD) Study of Low-Energy 1Ag-1T<sub>1u</sub> Transitions in Fullerene. *Chem. Phys.* **1993**, *172*, 277-283.
17. Stephens, P. J.; Schatz, P. N.; Ritchie, A. B.; McCaffery, A. J. Magnetic Circular Dichroism of Benzene, Triphenylene, and Coronene. *J. Chem. Phys.* **1968**, *48*, 132-138.
18. Stephens, P. J. Magnetic Circular Dichroism. *Annu. Rev. Phys. Chem.* **1974**, *25*, 201-232.
19. Seth, M.; Ziegler, T.; Autschbach, J. Ab Initio Calculation of the C/D Ratio of Magnetic Circular Dichroism. *J. Chem. Phys.* **2005**, *122*, 094112.
20. Solheim, H.; Ruud, K.; Coriani, S.; Norman, P. The A and B Terms of Magnetic Circular Dichroism Revisited. *J. Phys. Chem. A* **2008**, *112*, 9615-9618.
21. Seth, M.; Krykunov, M.; Ziegler, T.; Autschbach, J. Application of Magnetically Perturbed Time-Dependent Density Functional Theory to Magnetic Circular Dichroism. II. Calculation of A Terms. *J. Chem. Phys.* **2008**, *128*, 234102.
22. Seth, M.; Ziegler, T. Calculation of Magnetic Circular Dichroism Spectra with Time-Dependent Density Functional Theory. In *Advances in Inorganic Chemistry* VanEldik, R.; Harley, J., Eds. Elsevier Academic Press, Inc.: San Diego, 2010; Vol. 62, pp 41-109.
23. Solheim, H.; Ruud, K.; Coriani, S.; Norman, P. Complex Polarization Propagator Calculations of Magnetic Circular Dichroism Spectra. *J. Chem. Phys.* **2008**, *128*, 094103.
24. Lee, K. M.; Yabana, K.; Bertsch, G. F. Magnetic Circular Dichroism in Real-Time Time-Dependent Density Functional Theory. *J. Chem. Phys.* **2011**, *134*, 144106.

25. Štěpánek, P.; Bouř, P. Computation of Magnetic Circular Dichroism by Sum over States Summations. *J. Comput. Chem.* **2013**, *34*, 1531-1539.
26. Štěpánek, P.; Bouř, P. Origin-Independent Sum over States Simulations of Magnetic and Electronic Circular Dichroism Spectra Via the Localized Orbital/Local Origin Method. *J. Comput. Chem.* **2015**, *36*, 723-730.
27. Andersson, K.; Malmqvist, P. Å.; Roos, B. O. Second-Order Perturbation Theory with a Complete Active Space Self-Consistent Field Reference Function. *J. Chem. Phys.* **1992**, *96*, 1218-1226.
28. Ganyushin, D.; Neese, F. First-Principles Calculations of Magnetic Circular Dichroism Spectra. *J. Chem. Phys.* **2008**, *128*, 114117.
29. Yanai, T.; Kurashige, Y.; Mizukami, W.; Chalupský, J.; Lan, T. N.; Saitow, M. Density Matrix Renormalization Group for Ab Initio Calculations and Associated Dynamic Correlation Methods: A Review of Theory and Applications. *Int. J. Quantum Chem.* **2015**, *115*, 283-299.
30. Vitenberg, R.; Katz, B.; Scharf, B. The Assignment of the Benzene First-Ionization Rydberg Spectrum Via J-T Splittings Involving Linearly Inactive Modes. *Chem. Phys. Lett.* **1980**, *71*, 187-191.
31. Snyder, P. A.; Lund, P. A.; Schatz, P. N.; Rowe, E. M. Magnetic Circular Dichroism (MCD) of the Rydberg Transitions in Benzene Using Synchrotron Radiation. *Chem. Phys. Lett.* **1981**, *82*, 546-551.
32. Pantos, E.; Philis, J.; Bolovinos, A. The Extinction Coefficient of Benzene Vapor in the Region 4.6 to 36 Ev. *J. Mol. Spectrosc.* **1978**, *72*, 36-43.
33. Palmer, M. H.; Ridley, T.; Hoffmann, S. V.; Jones, N. C.; Coreno, M.; de Simone, M.; Grazioli, C.; Zhang, T.; Biczysko, M.; Baiardi, A.; Peterson, K. A. Combined Theoretical and Experimental Study of the Valence, Rydberg and Ionic States of Fluorobenzene. *J. Chem. Phys.* **2016**, *144*, 204305.
34. Padula, D.; Picconi, D.; Lami, A.; Pescitelli, G.; Santoro, F. Electronic Circular Dichroism in Exciton-Coupled Dimers: Vibronic Spectra from a General All-Coordinates Quantum-Dynamical Approach. *J. Phys. Chem. A* **2013**, *117*, 3355-3368.
35. Lin, N.; Solheim, H.; Zhao, X.; Santoro, F.; Ruud, K. First Principles Studies of the Vibrationally Resolved Magnetic Circular Dichroism Spectra of Biphenylene. *J. Chem. Theory Comput.* **2013**, *9*, 1557-1567.
36. Ferrer, F. J. A.; Santoro, F. Comparison of Vertical and Adiabatic Harmonic Approaches for the Calculation of the Vibrational Structure of Electronic Spectra. *Phys. Chem. Chem. Phys.* **2012**, *14*, 13549-13563.

37. Santoro, F.; Barone, V. Computational Approach to the Study of the Lineshape of Absorption and Electronic Circular Dichroism Spectra. *Int. J. Quantum Chem.* **2010**, *110*, 476-486.
38. Barone, V.; Bloino, J.; Biczysko, M.; Santoro, F. Fully Integrated Approach to Compute Vibrationally Resolved Optical Spectra: From Small Molecules to Macrosystems. *J. Chem. Theory Comput.* **2009**, *5*, 540-554.
39. Liu, Y.; Cerezo, J.; Mazzeo, G.; Lin, N.; Zhao, X.; Longhi, G.; Abbate, S.; Santoro, F. Vibronic Coupling Explains the Different Shape of Electronic Circular Dichroism and of Circularly Polarized Luminescence Spectra of Hexahelicenes. *J. Chem. Theor. Comput.* **2016**, *12*, 2799-2819.
40. Grimme, S.; Parac, M. Substantial Errors from Time-Dependent Density Functional Theory for the Calculation of Excited States of Large  $\pi$  Systems. *ChemPhysChem* **2003**, *3*, 292-295.
41. Frisch, M. J.; Trucks, G. W.; Schlegel, H. B.; Scuseria, G. E.; Robb, M. A.; Cheeseman, J. R.; Scalmani, G.; Barone, V.; Mennucci, B.; Petersson, G. A.; et al. *Gaussian 09*, Revision D01; Gaussian, Inc.: Wallingford CT, USA, 2009.
42. Cancès, E.; Mennucci, B.; Tomasi, J. A New Integral Equation Formalism for the Polarizable Continuum Model: Theoretical Background and Applications to Isotropic and Anisotropic Dielectrics. *J. Chem. Phys.* **1997**, *107*, 3032-3041.
43. Cardinal, J. R.; Mukerjee, P. Solvent Effects on the Ultraviolet Spectra of Benzene Derivatives and Naphthalene. Identification of Polarity Sensitive Spectral Characteristics. *J. Phys. Chem.* **1977**, *82*, 1614-1620.
44. Grimme, S.; Bannwarth, C. Ultra-Fast Computation of Electronic Spectra for Large Systems by Tight-Binding Based Simplified Tamm-Dancoff Approximation (sTDA-XTB). *J. Chem. Phys.* **2016**, *145*, 054103.
45. Kaminský, J.; Kříž, J.; Bouř, P. On the Magnetic Circular Dichroism of Benzene. A Density-Functional Study. *J. Chem. Phys.* **2017**, *146*, 144301.
46. Parr, R. G.; Yang, W. *Density-Functional Theory of Atoms and Molecules*. Oxford University Press: New York, 1994.
47. Štěpánek, P.; Cowie, T. Y.; Šafařík, M.; Šebestík, J.; Pohl, R.; Bouř, P. Resolving Electronic Transitions in Synthetic Fluorescent Protein Chromophores by Magnetic Circular Dichroism. *ChemPhysChem* **2016**, *17*, 2348–2354.
48. Finley, J.; Malmqvist, P.; Roos, B. O.; Serrano-Andrés, L. The Multi-State CASPT2 Method. *Chem. Phys. Lett.* **1998**, *288*, 299-306.
49. Widmark, P.; Malmqvist, P.; Roos, B. O. Density Matrix Averaged Atomic Natural Orbital (ANO) Basis Sets for Correlated Molecular Wave Functions. *Theor. Chem. Acc.* **1990**, *77*, 291-306.
50. Roos, B. The Complete Active Space Self-Consistent Field Method and Its Applications in Electronic Structure Calculations. *Adv. Chem. Phys.* **1987**, *69*, 399.

51. Marti, K. H.; Reiher, M., The Density Matrix Renormalization Group Algorithm in Quantum Chemistry. In *Z. Phys. Chem.*, 2010; Vol. 224, pp 583-599.
52. Kurashige, Y.; Chalupský, J.; Lan, T. N.; Yanai, T. Complete Active Space Second-Order Perturbation Theory with Cumulant Approximation for Extended Active-Space Wavefunction from Density Matrix Renormalization Group. *J. Chem. Phys.* **2014**, *141*, 174111.
53. Ghigo, G.; Roos, B. O.; Malmqvist, P. A Modified Definition of the Zeroth-Order Hamiltonian in Multiconfigurational Perturbation Theory (CASPT2). *Chem. Phys. Lett.* **2004**, *396*, 142-149.
54. Forsberg, N.; Malmqvist, P. Multiconfiguration Perturbation Theory with Imaginary Level Shift. *Chem. Phys. Lett.* **1997**, *274*, 196-204.
55. Sharp, T. E.; Rosenstock, H. M. Franck-Condon Factors for Polyatomic Molecules. *J. Chem. Phys.* **1964**, *41*, 3453-3463.
56. Santoro, F.; Improta, R.; Lami, A.; Bloino, J.; Barone, V. Effective Method to Compute Franck-Condon Integrals for Optical Spectra of Large Molecules in Solution. *J. Chem. Phys.* **2006**, *126*, 084509.
57. Zgierski, M. Z. Vibronic Structure of Mcd Spectra. I. Non-Condon Effects in Molecules with Nondegenerate Electronic States. *J. Chem. Phys.* **1985**, *83*, 2170-2185.
58. Furche, F.; Ahlrichs, R.; Wachsmann, C.; Weber, E.; Sobanski, A.; Vögtle, F.; Grimme, S. Circular Dichroism of Helicenes Investigated by Time-Dependent Density Functional Theory. *J. Am. Chem. Soc.* **2000**, *122*, 1717-1724.
59. Nakai, Y.; Mori, T.; Inoue, Y. Theoretical and Experimental Studies on Circular Dichroism of Carbo[N]Helicenes. *J. Phys. Chem.* **2012**, *116*, 7372-7385.
60. Lipkowitz, K. B.; Cundari, T. R.; Elliot, P.; Furche, F.; Burke, K. Excited States from Time-Dependent Density Functional Theory. In *Reviews in Computational Chemistry*, Lipkowitz, K. B.; Cundari, T. R., Eds. John Wiley & Sons, Inc.: Hoboken, New Jersey, 2009; Vol. 26, pp 91-165.
61. Schreiber, M.; Silva, M. R.; Sauer, S. P. A.; Thiel, W. Benchmarks for Electronically Excited States: CASPT2, CC2, CCSD, and CS3. *J. Chem. Phys.* **2008**, *128*, 134110.
62. Chai, J. D.; Head-Gordon, M. Systematic Optimization of Long-Range Corrected Hybrid Density Functionals. *J. Chem. Phys.* **2008**, *128*, 084106.
63. Rubio, M.; Merchán, M.; Ortí, E.; Roos, B. O. A Theoretical Study of the Electronic Spectrum of Naphthalene. *Chem. Phys.* **1993**, *179*, 395-409.
64. Vašák, M.; Whipple, M. R.; Michl, J. Magnetic Circular Dichroism of Cyclic  $\pi$ -Electron Systems. 7.<sup>1,2</sup> Analogues of Naphthalene. *J. Am. Chem. Soc.* **1978**, *100*, 6838-6843.
65. Goerigk, L.; Grimme, S. Efficient and Accurate Double-Hybrid-Meta-GGA Density Functionals-Evaluation with the Extended Gmtn30 Database for General Main Group

Thermochemistry, Kinetics, and Noncovalent Interactions. *J. Chem. Theory Comput.* **2011**, *7*, 291-309.

66. Chen, D.; Liu, J.; Ma, H.; Zeng, Q.; Liang, W. Analytical Derivative Techniques for TDDFT Excited-State Properties: Theory and Application. *Sci. China Chem.* **2014**, *57*, 48-57.

67. Frisch, M. J.; Trucks, G. W.; Schlegel, H. B.; Scuseria, G. E.; Robb, M. A.; Cheeseman, J. R.; Scalmani, G.; Barone, V.; Petersson, G. A.; Nakatsuji, H.; et al. *Gaussian 16*. Wallingford, CT, 2016.

68. Huebner, R. H.; Meilczarek, S. R.; Kuyatt, C. E. Electron Energy-Loss Spectroscopy of Naphthalene Vapor. *Chem. Phys. Lett.* **1972**, *16*, 464-469.

69. Dick, B.; Hohlneicher, G. Two-Photon Spectroscopy of the Low-Lying Singlet States of Naphthalene and Acenaphthene. *Chem. Phys. Lett.* **1981**, *84*, 471-478.

70. Biermann, D.; Schmidt, W. Diels-Alder Reactivity of Polycyclic Aromatic Hydrocarbons. 1. Acenes and Benzologs. *J. Am. Chem. Soc.* **1980**, *102*, 3163-3173.

**Table 1. Experimental and Calculated Band Positions in Naphthalene<sup>a</sup>**

		B3LYP vacuum		B3LYP CPCM		$\omega$ B97XD CPCM		LC-BLYP CPCM		CASPT2 vacuum		lit.	this work
		E	<i>f</i>	E	<i>f</i>	E	<i>f</i>	E	<i>f</i>	E	<i>f</i>		
1	$B_{3u}$	4.35 (3.95)	0.06	4.32	0.08	4.64	0.11	4.87	0.12	4.39	0.11	4.0 <sup>68</sup>	(4.34)
2	$B_{2u}$	4.44 (4.23)	0.00	4.44	0.00	4.61	0.00	4.72	0.00	4.20	0.00	4.45 <sup>68</sup>	(3.94)
3	$A_u$	5.25 (5.13)	0.00	5.30	0.00	5.99	0.00	6.22	0.00			5.6 <sup>68</sup>	
4	$B_{1g}$	5.50 (5.25)	0.00	5.67	0.00	6.39	0.00	6.65	0.00	6.02	0.00	5.22 <sup>69</sup>	
5	$B_{2g}$	5.57 (5.43)	0.00	5.63	0.00	6.44	0.00	6.70	0.00				
6	$B_{3g}$	5.60 (5.53)	0.00	5.49	0.00	6.08	0.00	6.28	0.00				
7	$B_{2u}$	5.85 (6.37)	1.25	5.63	1.46	5.83	1.54	6.01	1.60	5.87	1.46	6.0 <sup>68</sup>	
8	$B_{3u}$	6.00	0.01	6.00	0.26	6.26	0.00	6.45	0.46	5.96	0.29	5.89 <sup>68</sup>	(5.62)
9	$B_{1u}$	6.06 (5.51)	0.19	6.05	0.02	6.76	0.04	7.00	0.04				
10	$A_g$	6.11 (6.19)	0.00	6.11	0.00	6.43	0.00	6.71	0.00	6.01	0.00	5.52 <sup>69</sup>	
11	$B_{1u}$	6.17	0.02	6.24	0.02	7.05	0.02	7.35	0.02				
12	$A_u$	6.17	0.00	6.24	0.00	7.02	0.00	7.31	0.00				
13	$B_{1g}$	6.18	0.00	6.14	0.00	6.55	0.00	7.24	0.00	6.63	0.00	5.8 <sup>68</sup>	
14	$B_{3g}$	6.30	0.00	6.36	0.00	6.99	0.00	7.46	0.00				
15	$B_{2g}$	6.38	0.00	6.46	0.00	7.21	0.00	7.65	0.00				
16	$B_{3g}$	6.66	0.00	6.64	0.00	7.19	0.00	7.48	0.00				
17	$A_u$	6.70	0.00	6.68	0.00	7.24	0.00	7.47	0.00				
18	$B_{3g}$	6.79	0.00	6.87	0.00	7.70	0.00	8.06	0.00				
19	$A_g$	6.80	0.00	6.80	0.00	7.56	0.00	7.95	0.00	6.61	0.00	6.05 <sup>69</sup>	
20	$B_{2g}$	6.84	0.00	6.84	0.00	7.31	0.00	7.66	0.00				
	$\Delta$	0.37		0.42		0.75		1.02		0.44		0	

<sup>a</sup> Energies  $E$  are in eV, oscillator strengths  $f$  are dimensionless. The numbers in parentheses relate to transitions between vibrational ground states in the electronic ground and excited states ( $0 \rightarrow 0'$ ),  $\Delta$  is average absolute deviation from the experimental energies.

**Table 2. Experimental and Calculated Band Positions in Larger PAHs<sup>a</sup>**

		B3LYP vacuum		B3LYP CPCM		$\omega$ B97XD CPCM		LC-BLYP CPCM		CASP T2		lit.	this work
		E	f	E	f	E	f	E	f	E	f		
<b>anthracene:</b>													
1	$B_{1u}$	3.21 (2.90)	0.06	3.18	0.08	3.53	0.12	3.79	0.15	3.26	0.11	3.38 <sup>70</sup>	(3.31)
2	$B_{2u}$	3.84	0.00	3.84	0.00	4.04	0.00	4.13	0.00	3.73	0.00	3.57 <sup>70</sup>	
9	$B_{2u}$	5.14	1.99	4.89	2.26	5.14	2.38	5.33	2.47	5.23	2.08	4.86 <sup>70</sup>	4.92
13	$B_{1u}$	5.73	0.08	5.71	0.13	6.06	0.22	6.25	0.30	5.73	0.20		5.82
<b>phenanthrene:</b>													
1	$A_1$	3.94 (3.70)	0.00	3.94	0.00	4.25	0.00	4.45	0.00	3.96	0.00	3.63 <sup>70</sup>	(3.59)
2	$B_2$	4.19 (3.87)	0.06	4.17	0.11	4.51	0.14	4.71	0.11	4.43	0.09	4.23 <sup>70</sup>	(4.24)
3	$A_1$	4.68	0.10	4.64	0.15	5.20	0.28	5.65	0.36	4.75	0.30	4.93 <sup>70</sup>	4.82
4	$B_2$	4.88	0.62	4.76	0.89	5.14	1.20	5.36	1.29	5.21	1.26	5.30 <sup>59</sup>	4.94
<b>PAH4:</b>													
1	$B$	3.61 (3.37)	0.00	3.61	0.00	3.94	0.00	4.16	0.00	3.73	0.00	3.38 <sup>70</sup>	
2	$A$	3.70 (3.49)	0.02	3.69	0.03	4.09	0.03	4.32	0.02	3.95	0.03	3.84 <sup>70</sup>	
3	$B$	4.35 (4.02)	0.82	4.23	1.07	4.61	1.31	4.90	1.44	4.59	1.09	4.48 <sup>70</sup>	4.42
4	$A$	4.40	0.10	4.37	0.16	4.84	0.05	5.03	0.01	4.63	0.00		4.58
7	$B$	4.85	0.09	4.83	0.07	5.66	0.02	6.06	0.07	4.80	0.28		4.75
<b>PAH5:</b>													
1	$A$	3.35 (3.11)	0.00	3.35	0.00	3.71	0.00	3.94	0.00	3.65	0.00	3.20	
2	$B$	3.57 (3.31)	0.01	3.56	0.01	3.97	0.02	4.17	0.02	4.36	0.01		3.78
3	$B$	3.83 (3.67)	0.34	3.76	0.50	4.22	0.78	4.53	0.87	4.42	0.73		4.12
8	$B$	4.49	0.36	4.45	0.42	5.13	0.52	5.58	0.68	4.73	0.14		4.75
11	$B$	4.93	0.08							5.47	0.20		5.38
<b>PAH6:</b>													
1	$B$	3.21 (2.99)	0.00	3.21	0.01	3.58	0.00	3.81	0.00	3.62	0.00		
2	$A$	3.36 (3.06)	0.00	3.35	0.00	3.80	0.00	4.03	0.00	3.90	0.01		
3	$B$	3.63 (3.48)	0.34	3.57	0.45	4.01	0.58	4.32	0.64	4.14	0.58		3.59
4	$A$	3.74	0.05	3.73	0.09	4.23	0.02	4.48	0.01	4.22	0.01		3.99
18	$B$	5.00	0.20							4.88	0.18		4.90
25	$A$	5.27	0.13							6.03	0.19		5.40
$\Delta$		0.21		0.21		0.34		0.58		0.23			

<sup>a</sup> Selected transitions only (cf. Table S1 for complete list), the same layout as in **Table 2** is used. Transition numbering corresponds to the B3LYP TD DFT computation.

**Table 3. Naphthalene Bond Lengths<sup>a</sup> in Three Lowest-Energy Singlet States**

State	$d_{1,2}$	$d_{2,3}$	$d_{1,8a}$	$d_{4a,8a}$	$CH_1$	$CH_2$
S <sub>0</sub> , ground	1.375	1.415	1.420	1.432	1.085	1.084
S <sub>1</sub>	1.428	1.376	1.414	1.438	1.085	1.083
S <sub>2</sub>	1.400	1.426	1.413	1.486	1.085	1.083

<sup>a</sup> Atom numbering as in Table S3.

**2** (naphthalene)

**3a** (anthracene)

**3p** (phenanthrene)

**4** (3,4-benzophenanthrene)

**5** ([5]helicene)

**6** ([6]helicene)

**Figure 1.** Studied compounds.

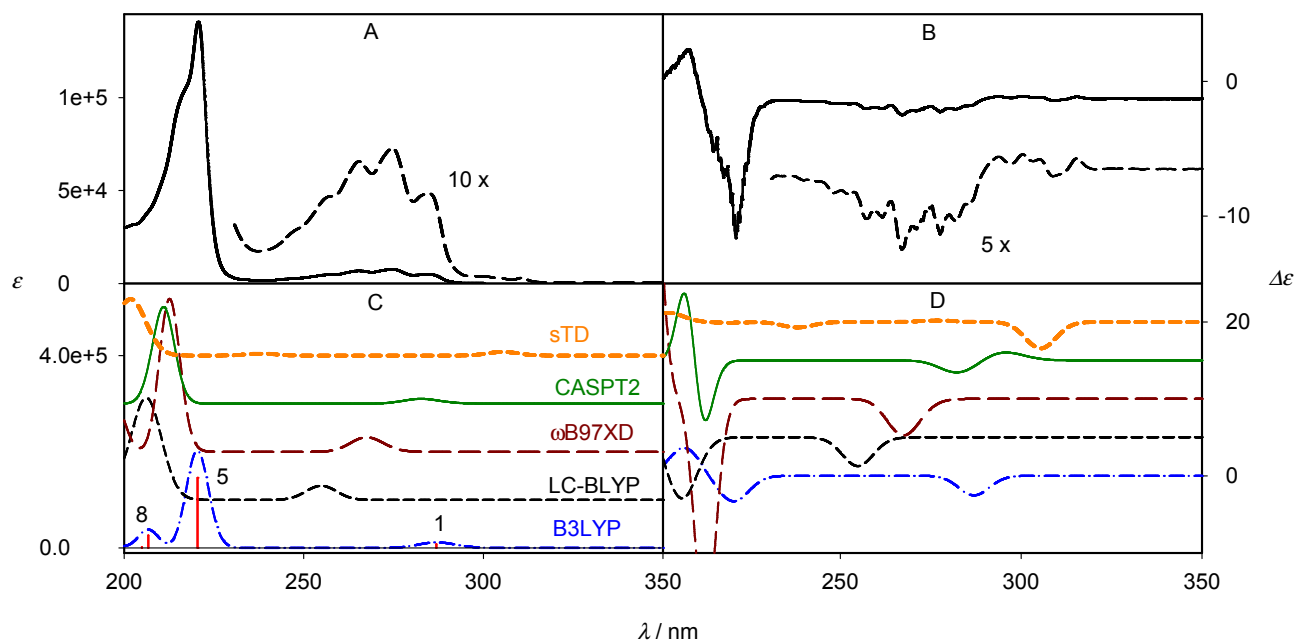


**Figure 2.** Naphthalene, experimental (A and B) absorption ( $\epsilon$ ) and MCD ( $\Delta\epsilon$ ) spectra, and theoretical curves obtained by five different methods (C and D), i. e., Tamm-Dancoff approximations<sup>44</sup> (sTD, with  $\omega$ B97X), CASPT2,  $\omega$ B97XD, LC-BLYP and B3LYP functionals.

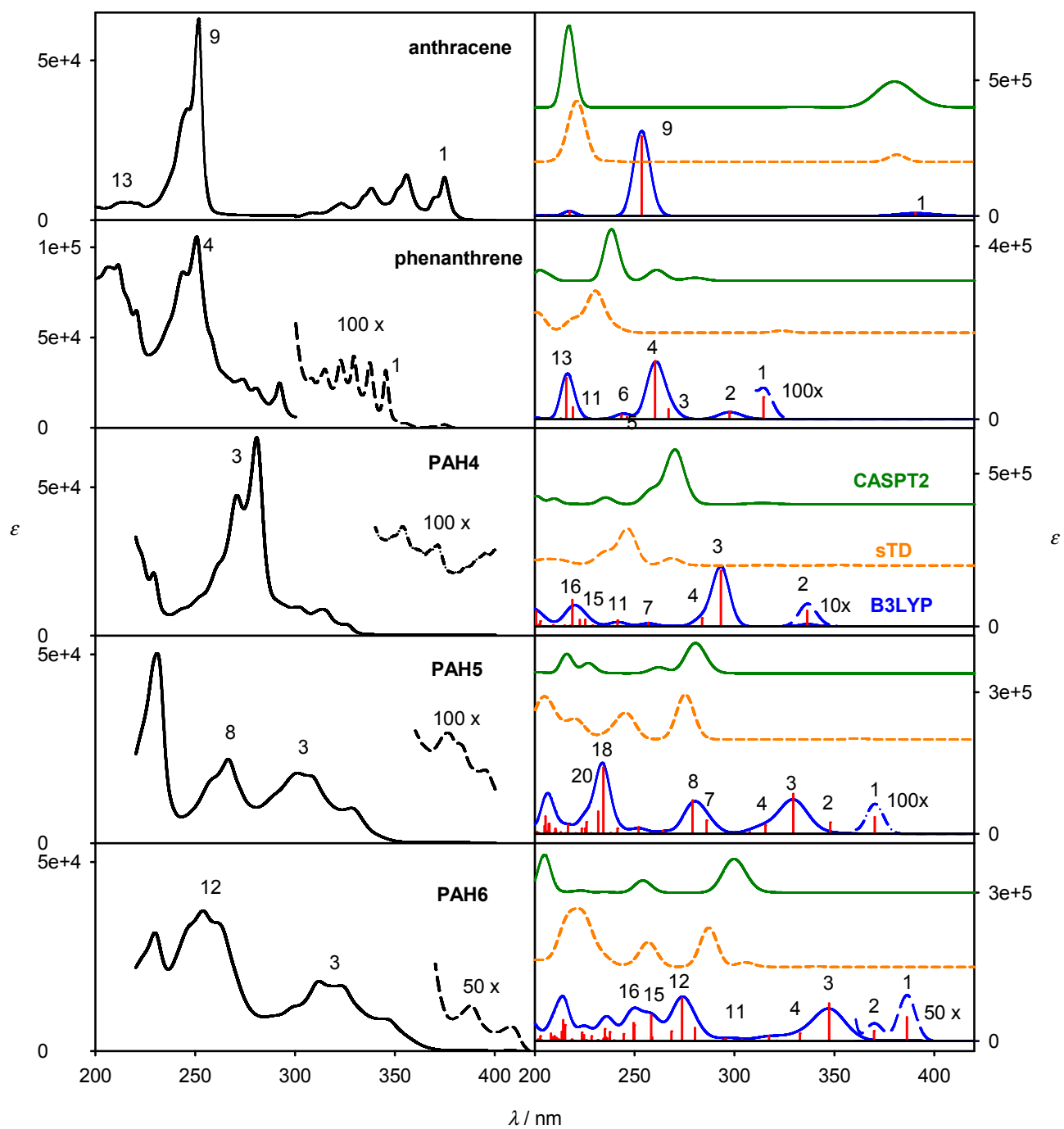


**Figure 3a.** Experimental (left) and calculated (right) absorption spectra of anthracene-PAH6.

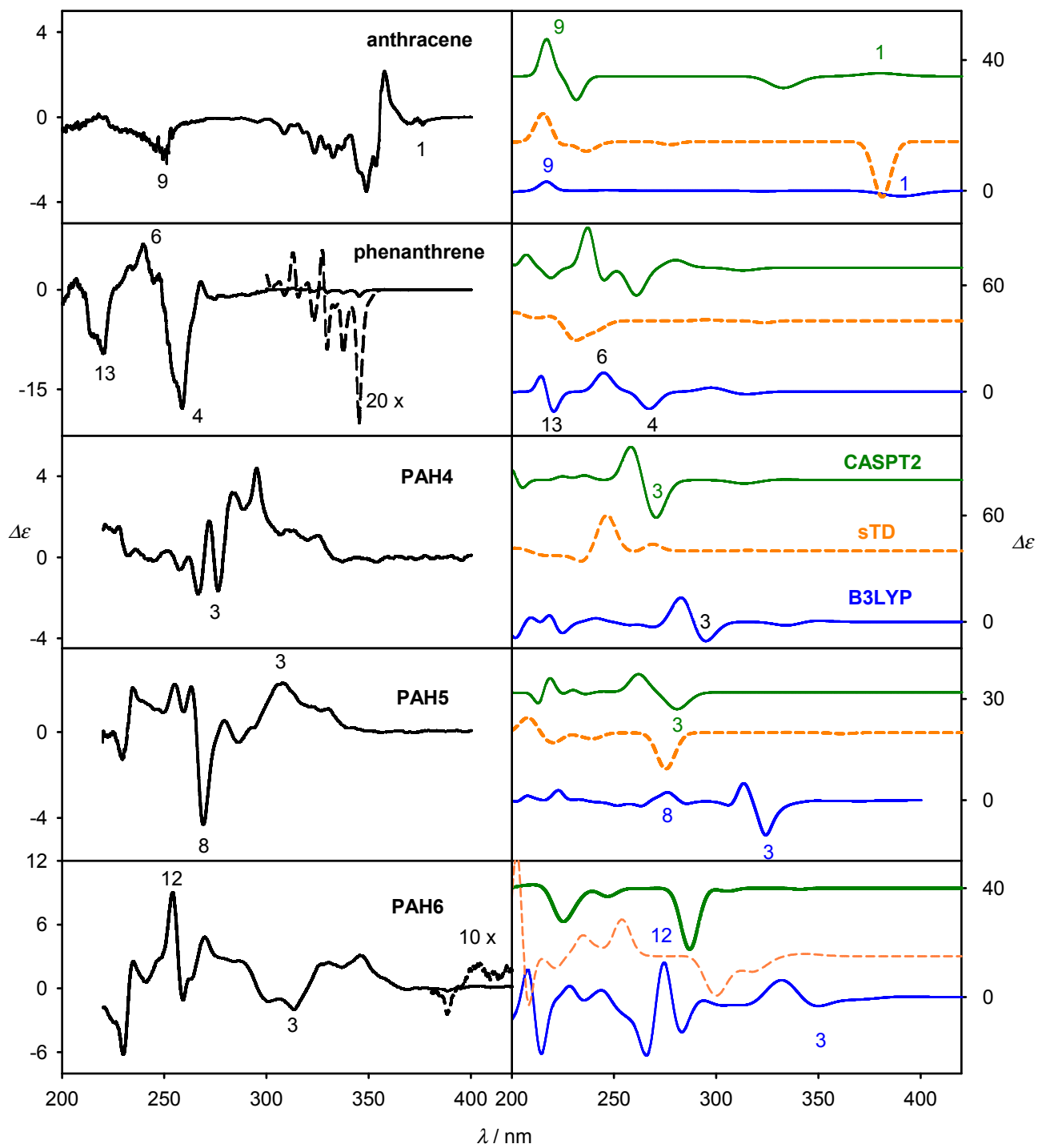


**Figure 3b.** Experimental (left) and calculated (right) MCD spectra of anthracene-PAH6.

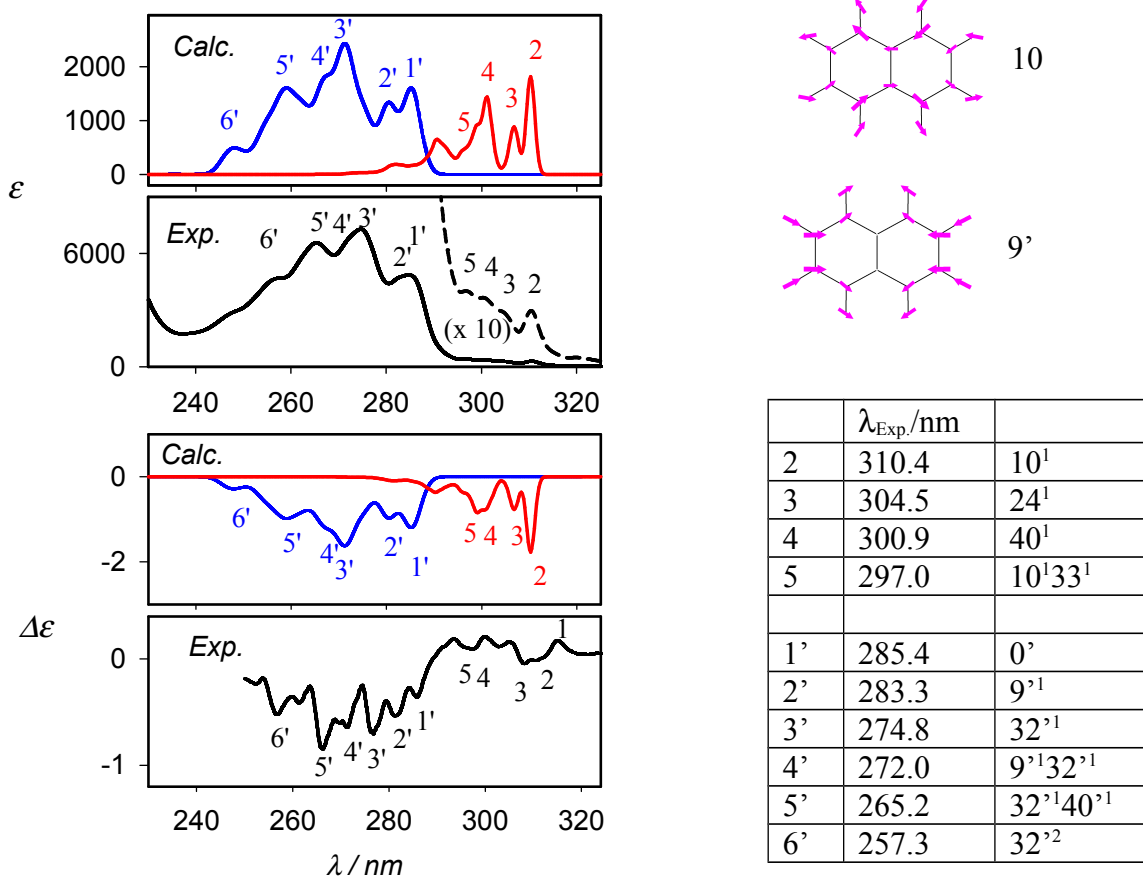


**Figure 4.** Vibrational structure in absorption and MCD spectra of naphthalene, experiment and computation. For easier comparison calculated spectra are shifted left by 29 nm ( $B_{3u}$ , blue) and 22 nm ( $B_{2u}$ , red). In the table on the right hand side, dominant transitions are listed; for example,  $32'^2$  means two excitations in the  $32^{\text{nd}}$  vibrational mode of the second (primed) electronic excited state. Normal mode displacements are displayed for vibrational modes 10 and  $9'$ .

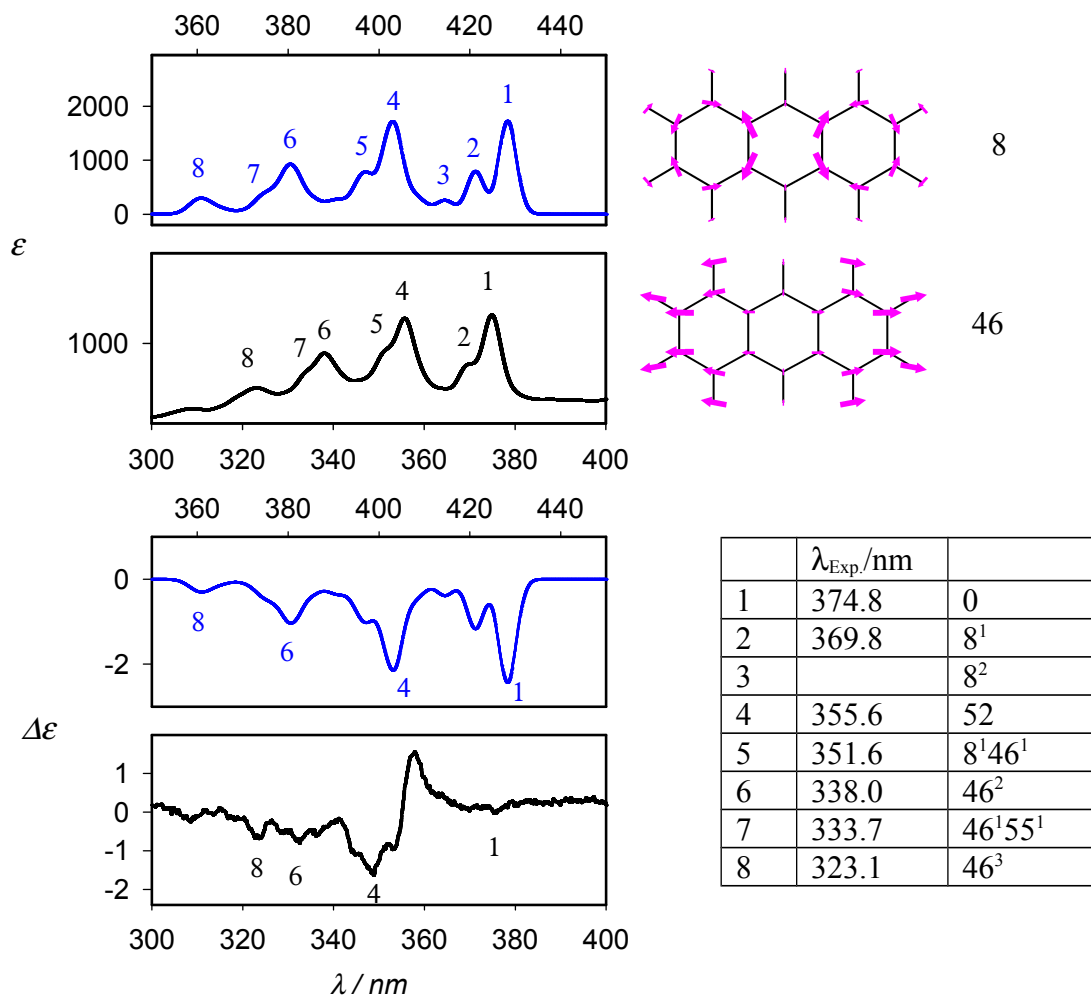


**Figure 5.** Vibrationally-resolved absorption and MCD spectra of anthracene  $S_0 \rightarrow S_1$  electronic transition. The dominant vibrational contributions are listed using the same notation as in Figure 4. Different wavelength scales are used for the experiment (black) and computation (blue). Around 358 nm (experimentally) the second electronic excited state interferes in the MCD spectrum.<sup>11</sup>

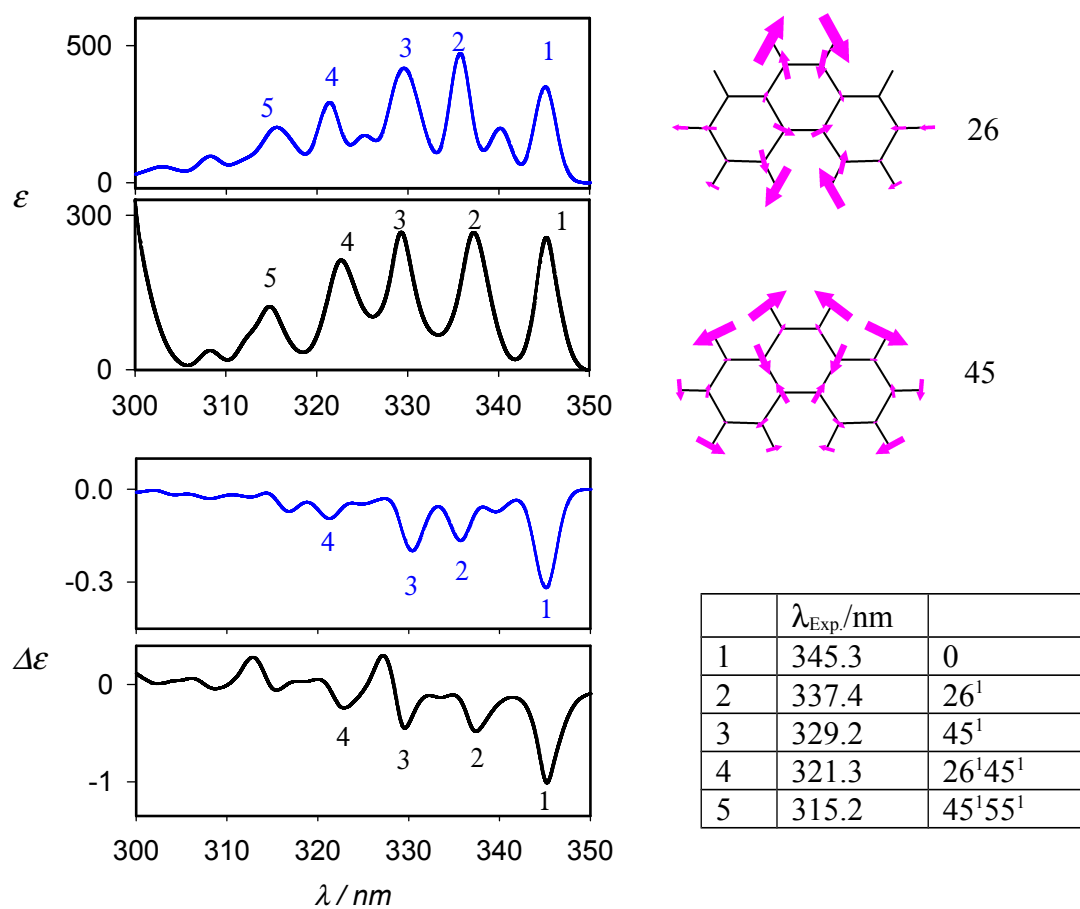


**Figure 6a.** Phenanthrene absorption and MCD spectra of the  $S_0 \rightarrow S_1$  transition, experiment is plotted in black (a polynomial baseline was subtracted from the absorption) and the computation in blue. Dominant vibrational contributions are listed using the same notation as in Figure 3. Calculated wavelengths are shifted by 10 nm to the right.

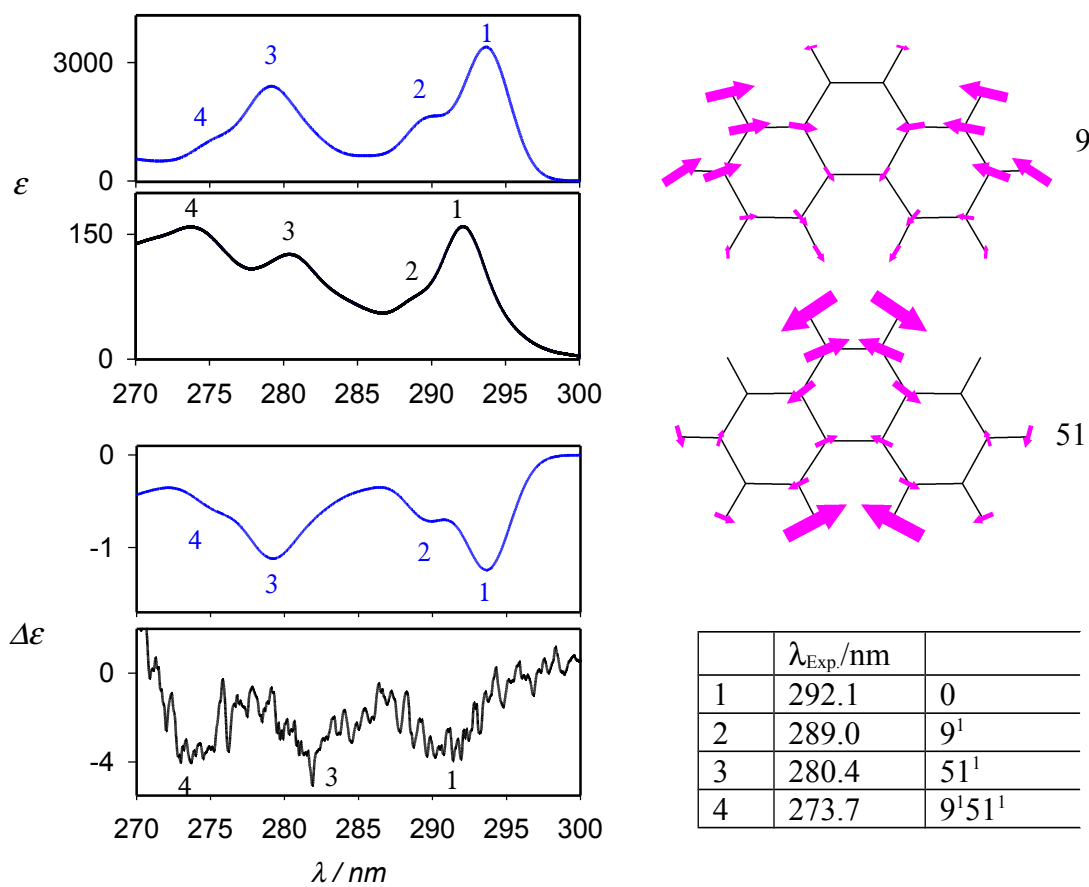


**Figure 6b.** Phenanthrene absorption and MCD spectra of the  $S_0 \rightarrow S_2$  transition, experiment is plotted in black and the computation in blue. Dominant vibrational contributions are listed using the same notation as in Figure 6a, calculated spectra are shifted by 29 nm to the left.

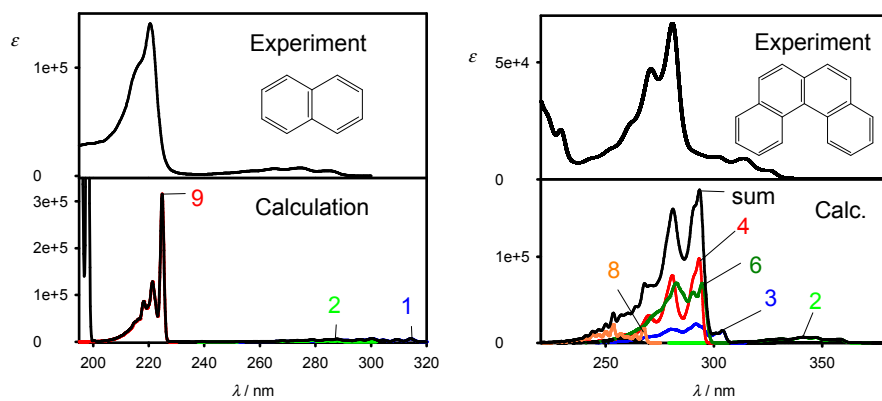


**Figure 7.** Absorption spectra of naphthalene and PAH4, experiment (top) and simulation including vibrational splitting (bottom).

# Table of Contents Graphic

